Coating of aluminum substrates with nanostructured Pd-Ni alloys by electrodeposition

Fernando Meneses[1,2], Julieta S. Riva[2], Silvia E. Urreta[1], Paula G. Bercoff[1,2] *

[1]Facultad de Matemática, Astronomía, Física y Computación (FAMAF), Universidad Nacional de Córdoba. Medina Allende s/n, Ciudad Universitaria, Córdoba, Argentina.

[2]Instituto de Física Enrique Gaviola (IFEG), CONICET, Medina Allende s/n, Ciudad Universitaria, Córdoba, Argentina.

*Corresponding author: Dr. Paula G. Bercoff. e-mail: bercoff@famaf.unc.edu.ar

Abstract

Pd-Ni alloys are electrodeposited onto low-purity aluminum substrates varying both the composition of the feeding solution and the applied electrodeposition potential. It is found that the initial nucleation-and-growth mechanism in every case is well described by a 3D-type nucleation process. The resulting deposits consist of Pd-Ni alloys of different compositions, all electrocrystallized in a disordered *fcc* phase; depending on the electrodeposition parameters, different morphologies and compositions are obtained. It is found that when the electrodeposition potential is high and the Pd content in the feeding solution is low, the substrate coating is more efficient and the deposit morphology tends to refine into dendritic-like structures, making this kind of deposit quite interesting for using as electrodes in electrochemical devices. Room temperature magnetic measurements indicate that the samples are soft ferromagnetic with negligible demagnetizing effects. Dendritic and spheroidal-like Pd-rich deposits exhibit larger remanence values and are more coercive than those with higher Ni content due to the dependence of the anisotropy constant on the alloy composition.

Keywords: Pd-Ni alloys; Electrodeposition; Aluminum substrate; Nucleation and growth mechanisms; Pd-Ni coating.

1. Introduction

Palladium is a noble metal with high catalytic activity, used in a large number of relevant reactions at industrial level. It is a performing material in various engineering and technological fields including catalysis [1-3], sensors [4,5], hydrogen storage [6] and in electronic and optoelectronic devices [7]. In particular, Pd-Ni alloys are good electron spin injectors and spin analyzers, being applied to the development of carbon nanotube-based electronics using electron spin ("spintronics").

These applications have stimulated extensive research interest on palladium nanoparticles [8,9], nanowires [10,11] and films [12-14], and on the processing routes to obtain these systems, which also offer a lower cost alternative to platinum. In this sense, the performance of palladium alloys with non-noble metals becomes important to reduce the catalyst cost.

Both the activity and stability of pure Pd need improvement, which can be achieved by combining it with other metals or metal oxides. It has been reported that modifications of Pd nanocatalysts with metals such as Ni effectively improve the catalytic performances toward alcohol oxidation in alkaline media [15-19]. For this reaction, the activity of catalysts prepared with Pd-Ni alloys of different compositions and morphologies, onto C-based supporting substrates, is found to be even larger than the corresponding to pure Pd [20-23]. Also, since Ni is a ferromagnetic material, another interesting aspect of Pd-Ni alloys is related to the possibility of synthesizing hard or soft nanomagnets either for technological [24] or medical applications [25]. H. Fujiwara

et al. [26] reported that the magnetocrystalline anisotropy constant in Pd-Ni alloys reaches a maximum value for 60 at. % Pd, conferring alloys close to this composition both the optimal characteristics for catalytic processes (because of the high Pd content) and a hard magnetic response. These combined properties are interesting for catalytic processes using Pd as catalyst, which can be improved using external magnetic fields [27].

Unsupported Pd-Ni particles have been synthesized to obtain efficient catalysts [28, 29]. However, C-based substrates are quite often used for electrodeposition of different Pd-Ni and noble-metal-containing nanostructures [21, 23]. Besides the C-based supports, different metals, alloys and oxides have also been used as substrates for electrodeposition of noble metals and bimetallic alloys nanostructures. In this sense, different authors report electrodeposition of Pd onto 316L stainless steel [30], Pd-Ni onto Ti [31], Cu onto Si [32], Ni-Co onto stainless steel [33], Pd-Ni onto Al_2O_3 [34] and Ag onto Indium Tin Oxide (ITO) [35], among others. On the other hand, the use of aluminum as a substrate is less common. The surface of metallic aluminum spontaneously oxidizes in the atmospheric environment. This oxidation creates a resistive film of native aluminum oxide, which affects negatively the electrodeposition of metals such as Cu, Ag and Ni. In industry this problem is solved by applying the zincate process [36] which improves the deposition of adhesive metallic films onto aluminum. Other strategies have been applied to improve adhesive properties of metal deposits on aluminum, such as pretreatments of the substrate surface [37], Ni plating [38] or slightly changing the composition of the aluminum substrate. However, little data exist related to the electrodeposition of Pd-Ni alloys onto aluminum substrates.

In this work, dc-electrodeposition of Pd-Ni alloys onto low-purity aluminum (98%) substrates has been performed. The influence of Ni concentration in the initial solution and the effect of the applied overpotential on the deposit properties are evaluated. Besides the magnetic properties of the samples, the interest is focused on the resulting deposit microstructure and composition, the extent of the substrate coverage and on its morphology, looking for a large active surface area to improve electrochemical performance.

2. Experimental procedures

Electrochemical depositions were performed onto square, plane and low-purity (98%) aluminum substrates 1 cm^2 in area. They were used as working electrodes in a three-electrode cell, with a saturated Ag/AgCl 3 M KCl electrode as reference and a Pt wire as counter electrode. Prior to the electrodeposition, the aluminum foils were degreased in acetone and ethanol for 10 minutes, then electro-polished in a mixture of $HClO_4$ and C_2H_5OH (1:3 volume ratio) at 16 V for 90 seconds, and finally rinsed with distilled water (Figure S1 shows images of the substrate before and after the electropolishing process). The electrodeposition processes were carried out at room temperature using an Autolab 302N (Metrohm) potentiostat/galvanostat, with NOVA 1.8™ data acquisition software at two deposition potentials: V_{ED} =-1.0 V and V_{ED} =-1.5 V, during an electrodeposition time t_{ED}= 1000 s.

Four sets of samples were prepared, each one from a given feed solution and electrodeposition potential. As indicated before, two values of V_{ED} were used: -1.0 V and -1.5 V, and two aqueous solutions with the same Pd concentration and different Ni concentrations were prepared: Ni-concentrated (0.06 M $NiSO_4$ + 0.01 M $PdCl_2$ + 0.3 M NH_4Cl + 1% v/v NH_4OH) and Ni-diluted (0.006 M $NiSO_4$ + 0.01 M $PdCl_2$ + 0.3 M NH_4Cl + 1% v/v NH_4OH). Before electrodeposition, these solutions were stirred with pure nitrogen.

The prepared samples were named Pd70-1.0V, Pd60-1.5V, Pd25-1.0V and Pd15-1.5V, where 70, 60, 25 and 15 refer to the atomic Pd content of the deposit, determined by large area EDS probing (the corresponding spectra are shown in Figure S2). Table 1 summarizes the electrodeposition parameters.

A Sigma Zeiss Field Emission - Scanning Electron Microscope (FE-SEM) was used to investigate the morphology of all samples using electron energy of 5 keV, final aperture of 30 μm and 2 mm focal distance. The samples composition was determined with an Oxford Energy-Dispersive Spectrometer (EDS) with an incident energy of 20 keV, involving large areas and several measurements in each sample. The crystallographic phases in the different deposits and the corresponding mean crystallite sizes were determined by X-ray diffraction (XRD) in a Philips PW 1800/10 X-ray diffractometer with Cu Kα radiation (λ = 1.540 Å).

Magnetic hysteresis loops were measured at room temperature in a Vibrating Sample Magnetometer (VSM) Lakeshore 7300 with a maximum applied field of 1.3 T.

Table 1. Sample denomination, electrodeposition conditions, and Pd at. % are listed. Experiments were conducted at room temperature, under an electrodeposition potential V_{ED} for 1000 s.

Sample	Ni Concentration [M] ([Pd]=0.01M)	V_{ED} [V]	Pd at. % [±3%]
Pd70-1.0V	0.006	-1.0	70
Pd60-1.5V	0.006	-1.5	60
Pd25-1.0V	0.060	-1.0	25
Pd15-1.5V	0.060	-1.5	15

3. Results and Discussion

3.1. Electrodeposition of Pd-Ni alloys

Due to their composition, the main species existing in the solutions are the complexes $Ni(NH_3)_6^{2+}$ and $Pd(NH_3)_4^{2+}$. In order to define the characteristics of the reduction process of these complexes, cyclic voltammograms (CVs) were recorded. Figure 1a shows the CVs of solutions with different $Ni(NH_3)_6^{2+}$ and $Pd(NH_3)_4^{2+}$ concentrations. The CV of the blank is also included, for comparison.

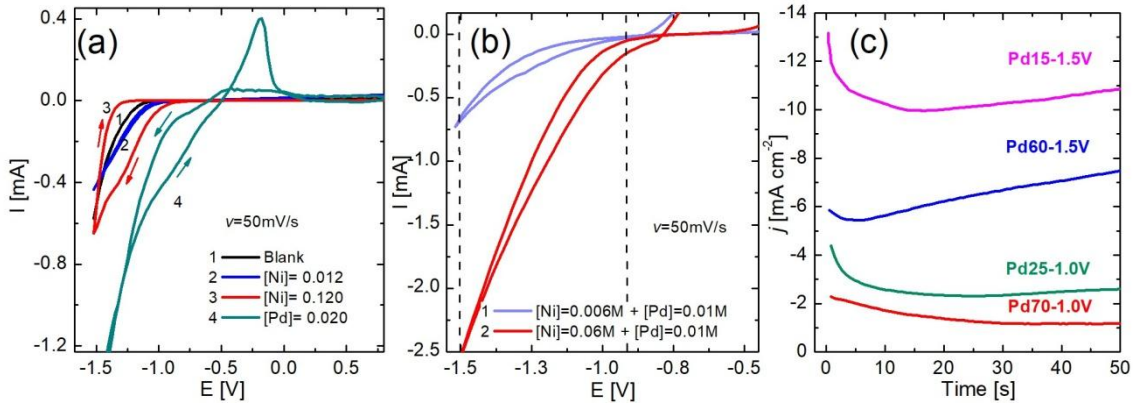

Figure 1. (a) Cyclic voltammograms for the supported electrolyte (Blank), for two Ni solutions, and for a Pd solution. Scan rate v= 50 mV/s. (b) Cyclic voltammograms for two Pd-Ni solutions of different Ni concentration. The vertical dashed lines indicate the potentials V_{ED} used for electrodeposition of the deposits. (c) Current-Time Transient (CTT) curves for the different deposits.

In the voltammogram of the Blank solution, the cathodic current increases sharply at about -1.1 V vs. Ag/AgCl, which is caused by hydrogen evolution. When $Ni(NH_3)_6^{2+}$ is present in the solution, the cathodic current starts to increase at somewhat lower potentials, -0.90 V and -0.80 V for $Ni(NH_3)_6^{2+}$0.006 M and 0.060 M respectively, indicating the reduction of Ni. The reverse scan shows a decrease in current density, and a crossover is observed with both Ni solutions, which is a characteristic feature of a metal deposition onto a substrate [39, 40]. It should be noted that there is not a peak in the positive scan, proving that Ni is not stripped from the electrode, even when anodic potentials of +1.0 V were applied.

The voltammogram for Pd is very similar to previously reported ones using stainless steel 316L [32] and gold [39] as working electrodes. The cathodic peak at -0.75 V is related to the reduction of the Pd complex $[Pd(NH_3)_4^{2+}] \rightarrow Pd^0$ [40]; this peak is immediately followed by an increase of the cathodic current which corresponds to hydrogen evolution. Also, it is known that the Pd hydride formation PdH_x occurs [41], but this

peak is usually hidden because of hydrogen evolution. In a reverse scan, the anodic peak corresponds to the oxidation of the absorbed hydrogen [40,41]. No other anodic peaks were observed during the scan, which indicates an irreversible electrodeposition process of Pd on the Al electrode.
From the previous CVs, two potentials for the electrodeposition processes were chosen,
V_{ED}=-1.0 V, where the nickel electrodeposition current begins to be observed, and V_{ED} = -1.5 V, where high currents are already observed, yet the evolution of hydrogen is also present.
Figure 1b shows the CVs corresponding to the two Pd-Ni solutions, where the chosen potentials are marked. The concentration of Pd was kept constant at 0.01 M while the concentration of Ni was 0.006 M in one solution and 0.060 M in the other. As it can be seen, there is a considerable increase of the cathodic current in the solution with the higher Ni concentration. In both CVs there is a crossover at around -0.8 V, which is indicative of an electrodeposition process.
The Current-Time Transient (CTT) curve was recorded during each electrodeposition. In order to describe the initial electro-crystallization kinetics, only the first 50 s of the CTT curves are analyzed, and the resulting current density *j vs.* time *t* graphs are plotted in Figure 1c. The current density is larger in the samples deposited at the higher potential, and for a given electrodeposition potential, it is larger in those with higher Ni concentration. The first effect is likely to arise from a driving force associated to the higher overpotential, while the second one is due to the presence of more ions in the electrolytic aqueous solutions.
Figure 1c shows that the experimental potentiostatic CCTs curves $j(t)$ exhibit an important current density at the beginning, arising from the double-charge layer building and a Langmuir-type ion adsorption–desorption processes j_{ad}, [42, 45]. This initial contribution may be described by the expression:

$$j_{ad}(t) = k_{ads}\, e^{-\,k_{des}\, t}, \tag{1}$$

with k_{ads} [mA·cm^{-2}] =A_{geom} (V_{ED}/*Rs*) the adsorption constant, and k_{des} [s^{-1}] = 1/*CRs* the desorption constant. Here V_{ED} is the electrodeposition potential, *Rs* is the solution resistance, *C* is the double layer capacitance, and A_{geom} is the surface area, such that $k_{ads} = k_{des} \cdot q_{ads}$, being q_{ads} [mC·cm^{-2}] the total charge for the adsorption process. As deposition time increases, a sequence of different nucleation processes may take place, but they are not identified in the present analysis and only a background is considered.

For single pure elements, the electrocrystalization mechanisms can be described considering a process involving the nucleation of the crystalline phase and further growth from the feed solution. One of the well-known theoretical models describing this process ─with nucleation of three-dimensional (3D) hemispherical nuclei followed by volume diffusion-controlled growth─ has been proposed by Scharifker-Hill (SH) [46], leading to the following expression for the current density:

$$j(t) = \left[\frac{zFD^{1/2}c}{\pi^{1/2}t^{1/2}}\right]\{1 - \exp\,[-N_0\pi kD(t - \tfrac{1-e^{-At}}{A})]\}, \tag{2}$$

were z represents the number of electrons, F is the Faraday constant, D is the diffusion coefficient, c is the concentration of the ion in the bulk, $k = (8\pi cM/\rho)^{1/2}$, M is the molar mass of the deposit, ρ is the density of the deposited material, A is the nucleation rate constant and N_0 is the number density of active sites.

The SH model considers two nucleation modes, progressive (P) and instantaneous (I). If the nucleation rate is high as compared to the growth rate, nuclei form at all possible growth sites within a short time and subsequent nucleation events take place on the deposit surface, leading to small grains. This is called a progressive (P) nucleation mode. However, if growth is easier than nucleation, nuclei forming at the substrate grow and prevent new nucleation events; this mode is termed instantaneous (I) [47]. It is possible that the nucleation regime changes from instantaneous to progressive during electrodeposition if the initially-deposited structures act as more friendly substrates for further nucleation.

Nucleation kinetics may be identified when the resulting experimental data are plotted in a dimensionless curve (j/j_{max}) *vs.* (t/t_{max}) and compared with the curves theoretically predicted by the SH model. Here, j_{max} is the maximum current value and t_{max} is the time at which this maximum is achieved. The theoretical adimensional curves proposed by Scharifker–Hill for instantaneous (3DI) and progressive (3DP) regimes [47] are:

$$\frac{j}{j_{max}} = \left(\frac{1.9542\; t_{max}}{t}\right)^{1/2}\left\{1 - exp\left[-1.2564\left(\frac{t}{tmax}\right)\right]\right\} \qquad \text{3DI} \tag{3}$$

$$\frac{j}{j_{max}} = \left(\frac{1.2254\, t_{max}}{t}\right)^{1/2} \left\{1 - exp\left[-2.3367\left(\frac{t}{tmax}\right)\right]\right\} \qquad \text{3DP} \qquad (4)$$

For electrodeposition of a bimetallic alloy (such as in the present case), Díaz-Morales et al. [48] have developed a model which accurately predicts the CTT curve for the alloy Hg-Ag. The expression for the nucleation/growth model for bimetallic phases proposed by these authors is:

$$J = \left[\frac{FD_w c^*}{\pi^{1/2} t^{1/2} D_a^{1/2}}\right]\{1 - \exp\left[-N_0 \pi k^* D_a^{\frac{1}{2}} D_w^{\frac{1}{2}}\left(t - \frac{1-e^{-At}}{A}\right)\right]\} \qquad (5)$$

where F is the Faraday constant, c^* is the pseudo-ion bulk concentration ($c^* = \gamma c_2 = c_1$), c_1 and c_2, are the bulk concentrations of the two metal ions, $D_w = \frac{z_1 D_1 \gamma + z_2 D_2}{\gamma(z_1 x_1 + z_2 x_2)}$, $D_a = \frac{(D_1 \gamma + D_2)}{(\gamma+1)}$, D_1 and D_2 are the diffusion coefficients of the two metal ions in the solution, z_1 and z_2 are the electron numbers of the two ions, $x_1 = \frac{c_1}{c_1+c_2}$ and $x_2 = \frac{c_2}{c_1+c_2}$, $k^* = [8\pi c^*(x_1 \frac{M_1}{\rho_1} + x_2 \frac{M_2}{\rho_2})]$, were M_1 and M_2 are the molar masses of the two metals and ρ_1 and ρ_2 are their densities. In this model, $D_w/D_a^{1/2}$ appears instead of $zD^{1/2}$ in the Scharifker-Hill model for a single element.

Thus, the dimensionless expressions derived from Eq. 5 are identical to Eqs. 3 and 4 from the Scharifker-Hill model for one kind of metallic ion. Therefore, Eqs. 3 and 4 can be applied to analyze the nucleation/growth process of bimetallic phases [44,48-52].

As mentioned above, in order to describe the initial electro-crystallization kinetics of the electrodeposited samples, only the first 50 s of the CTT curves are analyzed, considering a Langmuir-type initial contribution, and lognormal profiles for the nucleation processes. Figure 2 (left panel) shows the resulting experimental CCT curves and their fittings, showing two processes, P1 and P2.

Figure 2 (right panel) shows the dimensionless j/j_{max} *vs.* t/t_{max} curves calculated from data corresponding to the first maximum P1, observed up to 50 s. Table 2 also summarizes the values of the parameters corresponding to the initial Langmuir-like contribution, described by Eq. 1.

Table 2. Maximum current density j_{max}, time to maximum current density t_{max}, and the Langmuir-type contribution parameters (Eq. 1) obtained fitting the experimental CTTs depicted in Figure 2.

	t_{max}[s]	j_{max}[mA·cm^{-2}]	k_{ads} [mA·cm^{-2}]	k_{des} [s^{-1}]	q_{ads} [mC·cm^{-2}]
Pd70-1.0V	9	4.5	2.6	0.30	8.6
Pd60-1.5V	7	4.5	6.8	0.42	10.4
Pd25-1.0V	13	2.3	5.3	0.27	20.2
Pd15-1.5V	7	9	14	0.40	35.0

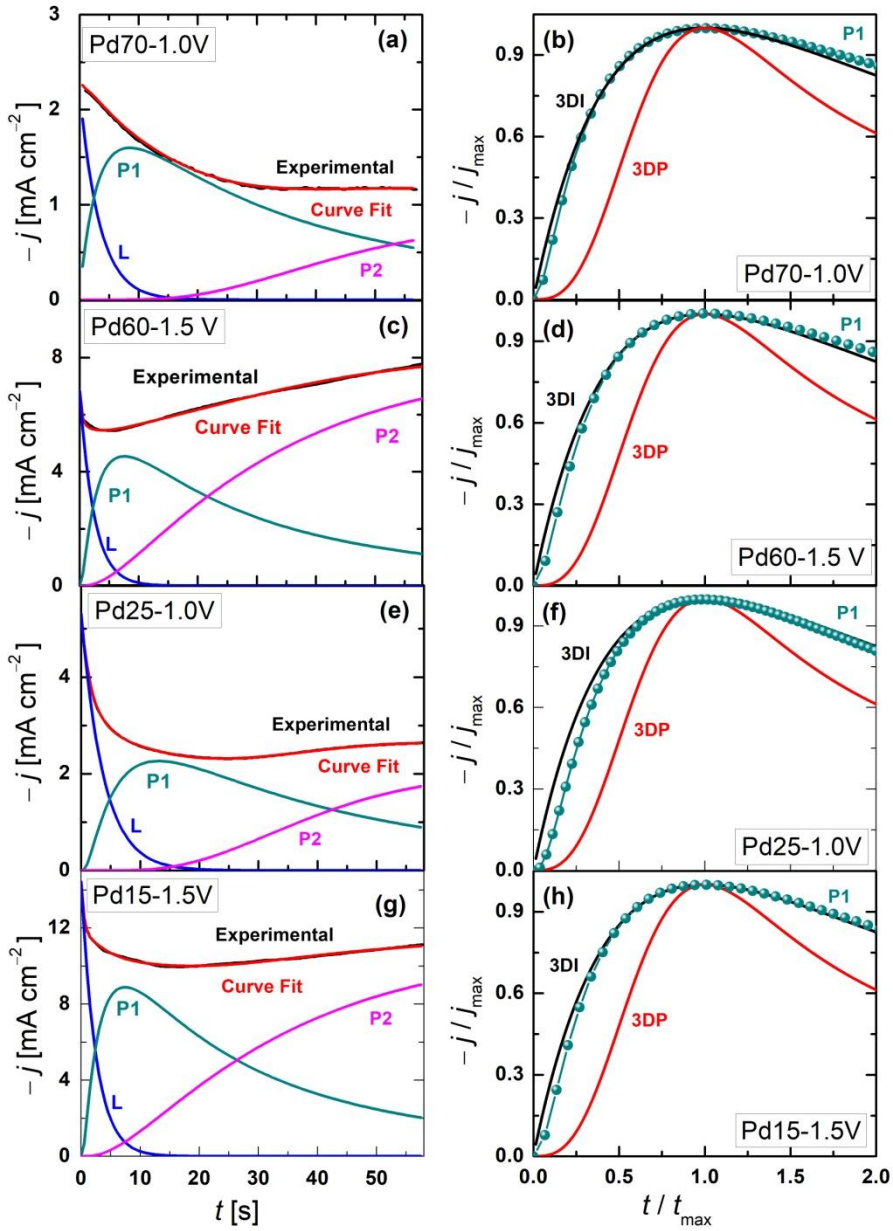

Figure 2. Left panel: CCTs fits to the experimental data. The function labeled j_{ad} corresponds to a Langmuir-like initial contribution, P1 is a first process which is further analyzed and P2 represents a background which is included for the fitting. Right panel: Dimensionless theoretical curves j/j_{max} *vs.* t/t_{max} corresponding to the mechanisms described by Eq. 3 (3DI) and Eq. 4 (3DP), together with those calculated from experimental data corresponding to the initial maximum P1, observed up to 50 s, for samples (a, b) Pd70-1.0V; (c, d) Pd60-1.5V; (e, f) Pd25-1.0V; and (g, h) Pd15-1.5V.

The analysis of the initial CCT curves resulting from the different applied potentials and feed solution compositions indicates that the initial crystallization rate is always controlled by ion diffusion in the solution volume. Also, in all the cases the early nucleation/growth mechanism is 3DI, even when a transition to a progressive regime 3DP cannot be excluded as deposition time increases. Similar evolution from an initial instantaneous to a progressive 3D mechanism has been reported for electrodeposition of Au onto Al substrates [53] and Cu onto glassy carbon [54] among others. It may be observed in Table 2 that the time to peak current

density t_{max} corresponding to the initial 3DI mechanism is slightly larger in deposits made at lower electrodeposition potential. The formation of the alloy phase depends on the competition between nucleation rate and nucleus growth, and the instantaneous nucleation tends to produce a solid solution alloy phase [46], so the nucleation model is consistent with the deposit characteristics, since the Pd-Ni electrodeposited layer is a solid solution alloy, as shown below.

3.2. Morphology and Microstructure

Figure 3a displays the diffractograms of the obtained deposits, which show that Pd and Ni ions crystallize forming a disordered *fcc* A1 (Pd,Ni) phase in every case [55-59]. Patterns of Pd-rich and Ni-rich samples were indexed following references PDF 00-005-0681 and PDF 00-004-0850, respectively. A progressive shift of the Pd-Ni peaks takes place when the Ni content is increased, with the lattice parameter following the Vegard law without significant deviations, as shown in Figure 3b. The mean lattice parameters for each composition were estimated by considering the *fcc* PdNi indexed peaks in Figure 3a and the values are listed in Table S1 (in the Supplementary Information). The assigned error corresponds to the respective standard deviation of these values. Even when the crystallite sizes d_{Sch} (estimated using the Scherrer formula and shown in Table S1) are similar for all the samples, the actual particle sizes observed in each morphology are dependent on the synthesis conditions, as it will be discussed later. The deposits crystallographic texture was evaluated using the expression $T(hkl) = \frac{I(hkl)/I_0(hkl)}{\frac{1}{N}\sum_{n=1}^{N} I(hkl)_n/I_0(hkl)_n}$ [60] where $I(hkl)$ and $I_0(hkl)$ are the peaks intensities corresponding to the (hkl) planes reflection in the sample and in the standard patterns, respectively, and N is the number of reflections (peaks) involved in the analysis. As shown by the results displayed in Table S1, all the deposits exhibit a slight (111) crystalline texture.

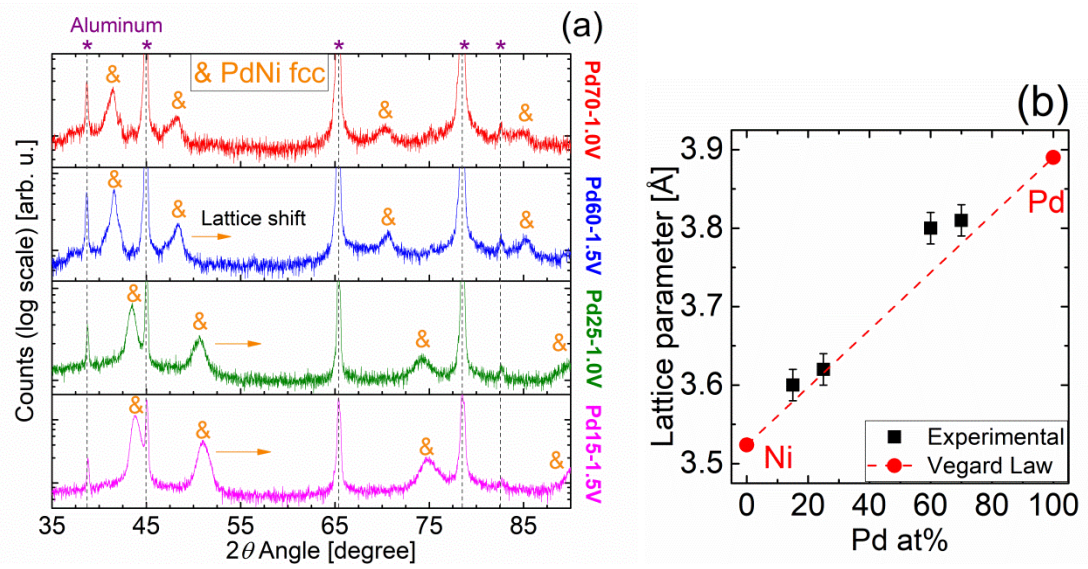

Figure 3. (a) X-ray diffractograms corresponding to the investigated samples, showing that they are single-phase in every case, with a pattern compatible with a disordered *fcc* A1(Pd,Ni) phase. The peaks marked with an asterisk and a dashed line correspond to the aluminum substrate. (b) Lattice parameter as a function of the Pd content, calculated from the diffractograms in (a).

The deposits onto the aluminum substrates, obtained after 1000 s of electrodeposition process under different conditions, are depicted in the images of Figure 4 to Figure 7. These deposits are not dense, continuous films, but a more or less uniform surface distribution of isolated microstructures. The substrate coating is more efficient in samples with high Ni content and in those processed at -1.5 V. The main parameter determining the morphology of these structures is the electrodeposition potential. In the case of V_{ED} = -1.0 V, agglomerates involving a few hemispherical particles are observed for both compositions, as shown in Figure 4 and Figure

6. In the case of the higher potential, V_{ED} = -1.5 V, no single particles are observed but dendritic-like structures with appreciable vertical development. In addition to the influence of the potential, the effect of solution composition is also noticeable. This has been checked in several samples with different deposition conditions (not discussed in this paper) and a comparison is shown in Figure S3. In the cases of low electrodeposition potential, samples with higher Pd content exhibit agglomerates ~12 μm in size, containing round particles ~3 - 6 μm in diameter. Similar agglomerates are observed in samples with lower Pd content but they are more densely distributed on the substrate. Then, decreasing the Pd content in the alloy (Ni-rich feeding solution) leads to more densely distributed structures, covering the substrate to a larger extent, suggesting that Ni promotes an easier nucleation stage.

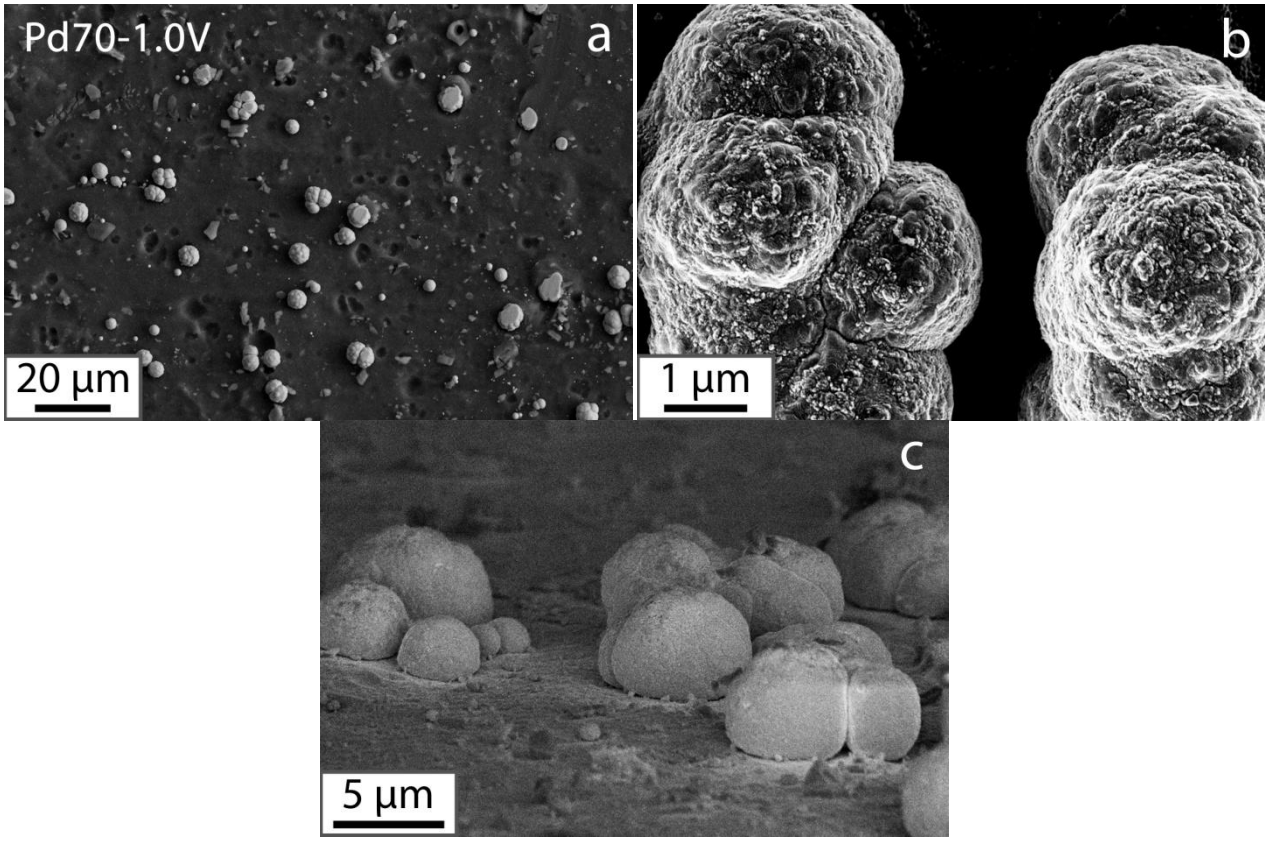

Figure 4. SEM images showing: (a, b) top and (c) lateral views of sample Pd70-1.0V.

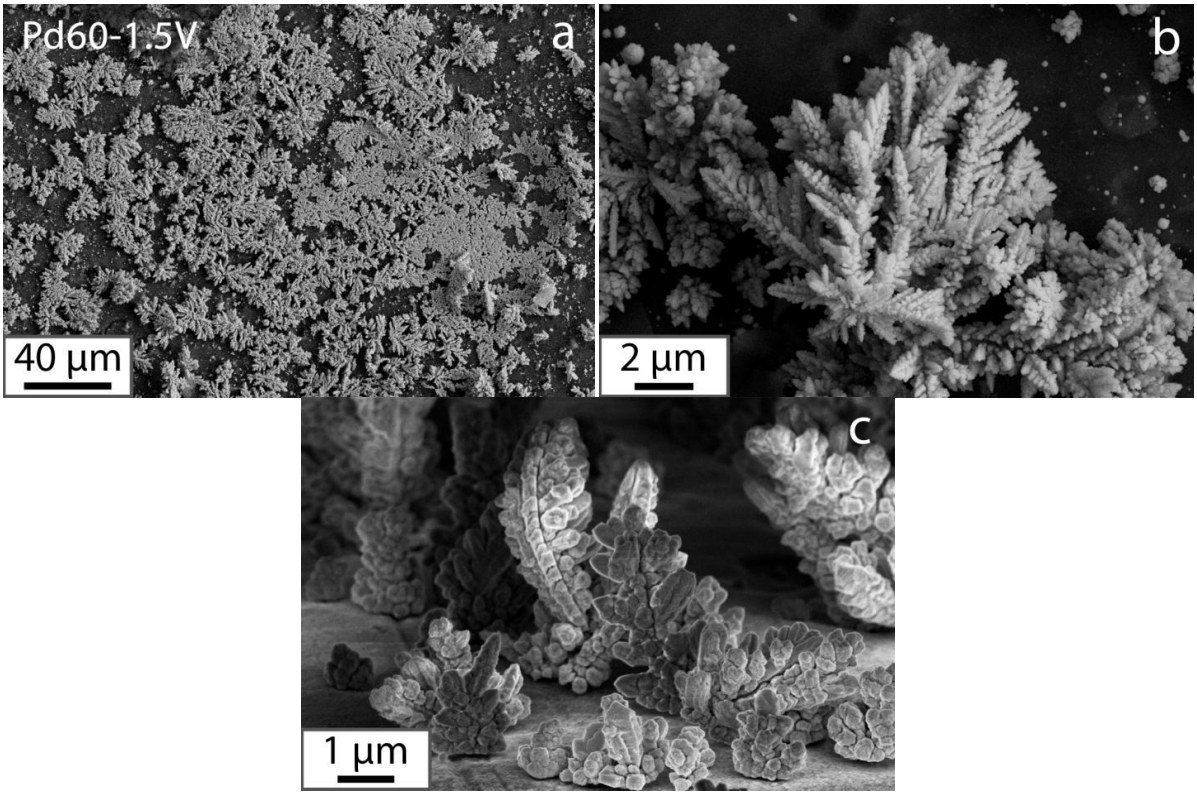

Figure 5. SEM images showing: (a, b) top and (c) lateral views of sample Pd60-1.5V.

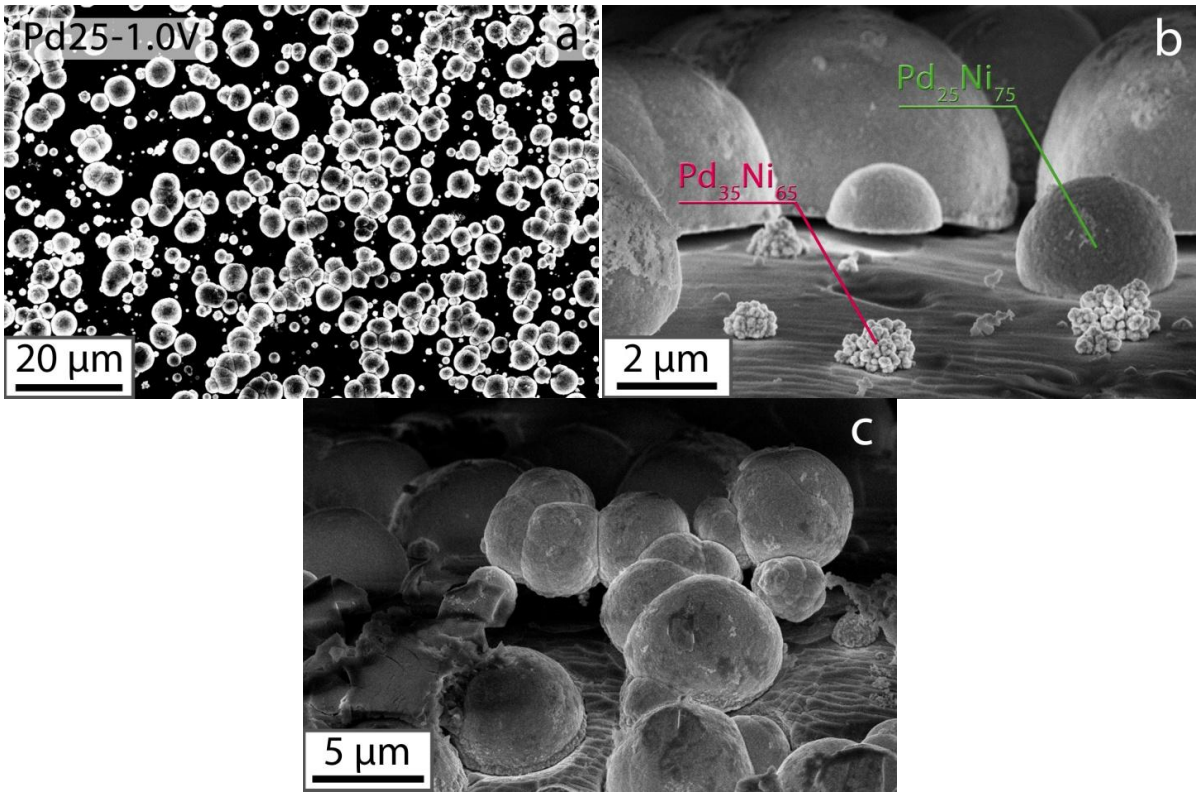

Figure 6. SEM images showing: (a) top and (b, c) lateral views of sample Pd25-1.0V. In (b), several agglomerates of Pd-rich nanoparticles coexisting with larger hemispheres of composition close to the mean one may be noticed.

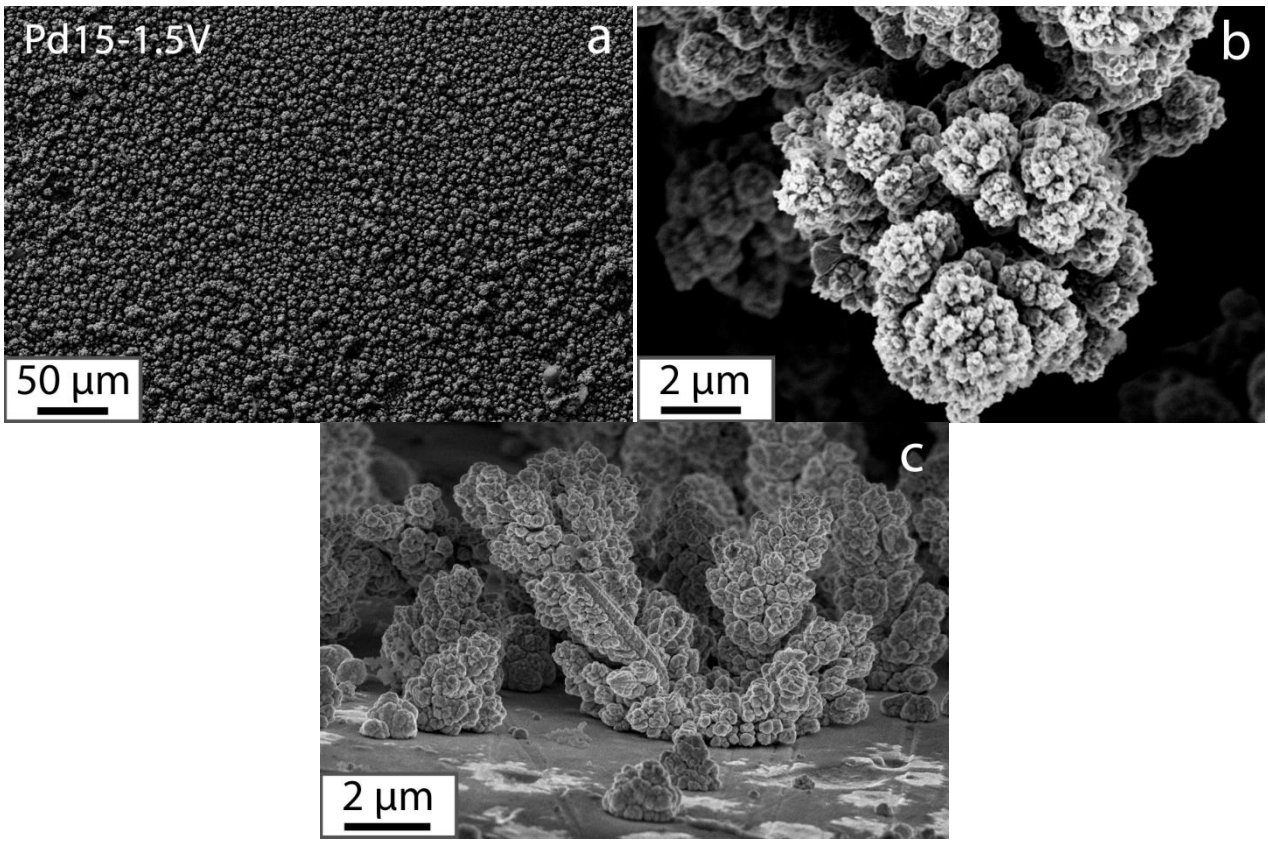

Figure 7. SEM images showing: (a, b) top and (c) lateral views of sample Pd15-1.5V.

When the electrodeposition potential is -1.5 V, dendritic-like structures are built up (see Figure 5 and Figure 7). It may be observed that in the Pd dilute alloy, the dendrite branches actually consist of small spherical particles pile-ups (corncob-like) leading to the observed 3D nanostructure [61]. Dendritic growth is understood on the basis of the competing influences of reaction rate, electrolyte transport rate, and self-diffusion barrier. Ramified or dendritic microstructures provide an increased surface-to-volume ratio as compared to the same volume of the particulate material. Surfaces of such microstructures will have regions or directions of greater curvature that may allow larger molecules to pack in a less crowded manner, making terminal functional groups or binding sites more accessible, as observed ─for instance─ in dendritic gold nanostructures onto fluorine-doped tin oxide (FTO)-coated glass [60]. The very open and porous structures here obtained may be considered as interesting electrodes in electrochemical devices.
Figure 6b depicts a portion of sample Pd25-1.0V where two distinct morphologies are observed. EDS elemental analyses performed on each of these structures give different values for the corresponding compositions. Agglomerates of quite small (20-40 nm) particles with composition Pd 35 at. % coexist with relatively large hemispheres of average composition near 25 at. % Pd, which is very close to the nominal deposit composition. These agglomerates of small particles are likely to nucleate and grow after Ni-rich hemispheres develop to a certain extent, leaving the feeding solution enriched in Pd. The morphology of the agglomerates confirms that new Pd-rich crystals nucleate preferably onto previous crystallized particles of the same phase and neither onto the Ni-rich phase nor onto the substrate. It is also observed that Pd refines the particle size.

3.3. Magnetic hysteresis properties

Magnetic hysteresis loops measured at room temperature are shown in Figure 8. All the loops are well described by the superposition of two contributions: a paramagnetic component arising from the aluminum substrate and a soft ferromagnetic one, from the Pd-Ni deposit. The coercivity and the reduced remanence (=

J_R/J_S with J_R and J_S the remanent and saturation polarizations, respectively) are somewhat larger in samples containing more Pd. This behavior may be explained by considering that the magnetocrystalline anisotropy constant in the Pd-Ni alloy reaches a maximum value near the composition $Pd_{65}Ni_{35}$ [26] in which range are samples Pd70-1.0V and Pd60-1.5V. Almost no difference is observed between the loops measured with the field applied normal (out of plane) and parallel (in plane) to the substrate plane, indicating that geometric demagnetizing effects are not significant. This behavior may be expected in these samples, where no dense coating of the substrate is observed, but layers with quite open or even isolated structures.

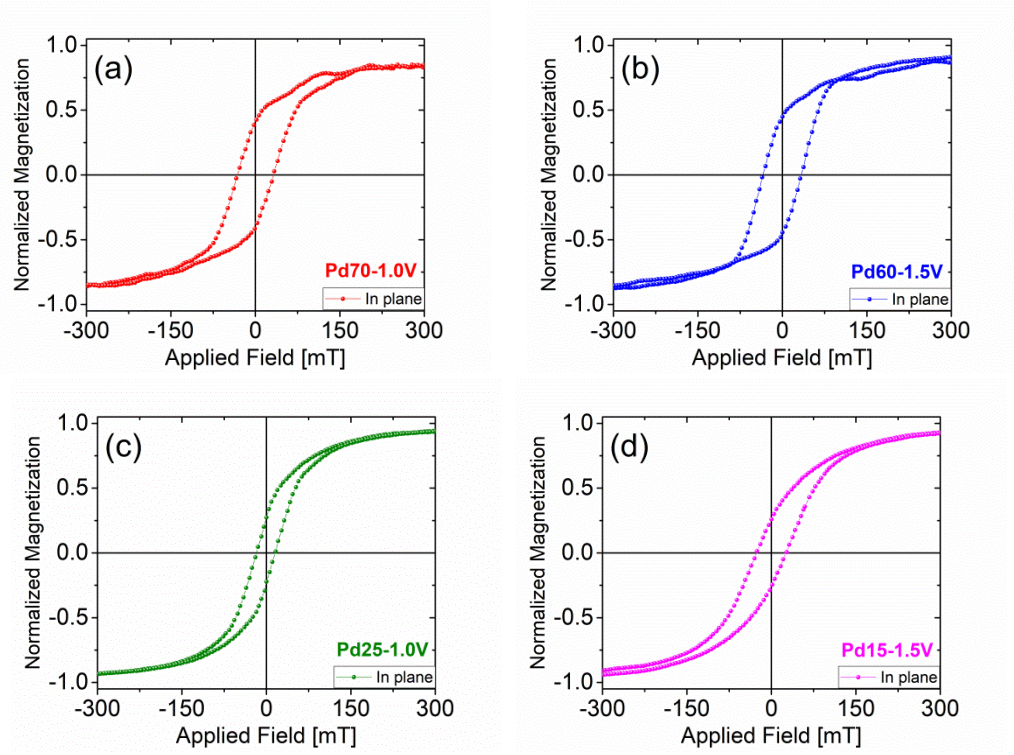

Figure 8. Room temperature hysteresis loops of samples (a) Pd70-1.0V, (b) Pd60-1.5V (c) Pd25-1.5V and (d) Pd15-1.5V.

4. Conclusion

Different Pd-Ni alloys crystallizing in a disordered *fcc* phase were electrodeposited onto low-purity Al substrates, obtaining distinct morphologies and compositions depending on the synthesis conditions. It is concluded that the main parameter determining both, the deposits morphology and composition, is the electrodeposition potential. For low electrodeposition potential values, the alloy crystallizes forming agglomerates of a few hemispherical particles onto the substrate. For high voltage values, dendrite-like, piled-up structures develop. The electrolytic bath concentration also influences the deposits morphology, leading to more densely distributed structures when Pd content is lower, indicating that Ni facilitates the nucleation process. The predominant nucleation and growth mechanism at the earlier stages of the electrodeposition is 3DI in every studied case. Magnetic characterization of the deposits indicates that geometric demagnetizing effects are not significant, in agreement with a sparse coating of the substrate, with quite separated or even isolated structures. Moderate values of coercivity are found (20-40 mT), indicating that the film magnetic configuration is not sensitive to the application of a small external magnetic field.

The dendritic-like microstructures obtained offer larger exposed areas than smooth surfaces, making this kind of deposits quite interesting for use in several potential applications. In fact, different electrochemical reactions could be enhanced when using this type of materials as electrodes in electrochemical devices, either for the hydrogen evolution reaction, for formic acid oxidation or for the 4-nitrophenol reduction reaction. We intend to explore some of them in future work.

Acknowledgements

This work has been partially funded by Universidad Nacional de Córdoba (SeCyT) and ANPCyT-Foncyt (Argentina). F. M. acknowledges a doctoral fellowship from CONICET.

References

(1) Díaz, R.; Arbiol, J.; Cirera, A.; Sanz, F.; Peiro, F.; Cornet, A.; Morante, J. R., Electroless Addition of Catalytic Pd to SnO_2 Nanopowders. *Chem. Mater.*13 (2001) 4362-4366.

(2) Gimeno, Y.; Creus, A. H.; González, S.; Salvarezza, R. C.; Arvia, A. J., Preparation of 100−160 nm-Sized Branched Palladium Islands with Enhanced Electrocatalytic Properties on HOPG. *Chem. Mater.* 13 (2001) 1857-1864.

(3) Ohno, S.; Wilde, M.; Mukai, K.; Yoshinobu, J.; Fukutani, K., Mechanism of Olefin Hydrogenation Catalysis Driven by Palladium-Dissolved Hydrogen. *J. Phys. Chem. C.* 120 (2016) 11481-11489.

(4) Favier, F.; Walter, E. C.; Zach, M. P.; Benter, T.; Penner, R. M. Hydrogen sensors and switches from electrodeposited palladium mesowire arrays. *Science* 293 (2001) 2227-2231.

(5) Bera, D.; Kuiry, S. C.; Patil, S.; Seal, S. Palladium nanoparticle arrays using template-assisted electrodeposition. *Appl. Phys. Lett.* 82 (2003) 3089-3091.

(6) Bemis, J. M.; Dahl, L. F., $H_{12}Pd_{28}(PtPMe_3)(PtPPh_3)_{12}(CO)_{27}$, a High-Nuclearity $Pd_{28}Pt_{13}$ Cluster Containing 12 Hydrido Atoms: A Possible Molecular Hydrogen-Storage Model for Palladium Metal. *J. Am. Chem. Soc.* 119 (1997) 4545-4546.

(7) Rani, J. R.; Oh, J.; Park, J.; Lim, J.; Park, B.; Kim, K.; Kim, S-J.; ChanJun, S. Controlling the luminescence emission from palladium grafted graphene oxide thin films via reduction. *Nanoscale*, 5 (2013) 5620-5627.

(8) Aguirre, M. C.; Rivas, B. L.; Fabietti, L. M.; Urreta, S. E. Enhanced performance of nano-electrocatalysts of Pd and PdCo in neutral and alkaline media. *J. Appl. Electrochem.* 49 (2019) 1–15.

(9) Kohsuke, Mori, M.; Salinas-Torres, D.; Kuwahara, Y.; Yamashita, H.; New approaches towards the Hydrogen production from formic acid dehydrogenation over Pd-based heterogeneous catalysts. *Frontiers in Materials*, 6 (2019) 1-8.

(10) Cheng, F.; Wang, H.; Sun, Z.; Ning, M.; Cai, Z.; Zhang, M., Electrodeposited fabrication of highly ordered Pd nanowire arrays for alcohol electrooxidation. *Electrochem. Commun.* 10 (2008) 798–801.

(11) Kim, M. J.; Cruz, M. A.; Yang, F.; Wiley, B. J., Accelerating electrochemistry with metal nanowires. *Curr. Opin. Electrochem.* 16 (2019) 19–27.

(12) Jia, F.; Wong, K.; Zhang, L., Electrochemical synthesis of nanostructured Palladium of different morphology directly on Gold substrate through a cyclic deposition/dissolution route. *J. Phys. Chem. C.* 113 (2009) 7200–7206.

(13) Iqbal, M.; Kaneti, Y. V.; Kashimura, K.; Yoshino, M.; Jiang, B.; Li, C.; Yuliarto, B.; Bando, Y.; Sugahara, Y.; Yamauchi, Y., Continuous mesoporous Pd films with tunable pore sizes through polymeric micelle-assisted assembly. *Nanoscale Horiz.* 4 (2019) 960-968.

(14) Schaltin, S.; Brooks, N. R.; Sniekers, J.; Van Meervelt, L.; Binnemans, K.; Fransaer, Jan., Electrodeposition of thick palladium coatings from a palladium(II)-containing ionic liquid. *Chem. Commun.* 50 (2014) 10248-10250.

(15) Ahmed, M. S.; Jeon, S., Highly Active Graphene-Supported Ni_xPd_{100-x} Binary Alloyed Catalysts for Electro-Oxidation of Ethanol in an Alkaline Media. *ACS Catalysis* 4 (2014) 1830-1837.

(16) Maiyalagan, T.; Scott, K. Performance of carbon nanofiber supported Pd–Ni catalysts for electro-oxidation of ethanol in alkaline medium. *J. Power Sources* 195 (2010) 5246–5251.

(17) Obradovic, M. D.; Stancic, Z. M.; Lacnjevac, U. C.; Radmilovic, V. V.; Gavrilovic-Wohlmuthere, A.; Radmilovic, V. R.; Gojkovic, S. Lj. Electrochemical oxidation of ethanol on palladium-nickel nanocatalyst in alkaline media. *Appl. Catal. B.* 189 (2016) 110–118.

(18) Miao, B.; Wu, Z-P.; Zhang, M.; Chen, Y.; Wang**, L.** Role of Ni in Bimetallic PdNi Catalysts for Ethanol Oxidation Reaction. *Phys. Chem. C.* 122 (2018) 22448-22459.

(19) Del Rosario, J. A.; Ocon, D. O.; Yi, H. J. Y.; Lee, J. W.; Lee. J., Enhancing role of nickel in Nickel-Palladium bilayer for electrocatalytic oxidation of ethanol in alkaline media. *J. Phys. Chem.* C 118 (2014) 22473-22478.
(20) Du, C.; Chen, M.; Wang, W.; Yin, G.; Shi, P., Electrodeposited PdNi2 alloy with novelly enhanced catalytic activity for electrooxidation of formic acid. *Electrochem. Comm.* 12 (2010) 843-846.
(21) Shen, S. Y.; Zhao, T. S.; Xu, J. B. Carbon-supported bimetallic PdIr catalysts for ethanol oxidation in alkaline media. *Electrochim. Acta* 55 (2010) 9179-9184.
(22) Tan, J. L.; De Jesús, A. M.; Chua, S. L.; Sanetuntikul, J.; Shanmugam, S.; Tongol, B. J. V.; Kim, H., Preparation and characterization of palladium-nickel on graphene oxide support as anode catalyst for alkaline direct ethanol fuel cell. *Appl. Catal. A.* 531 (2017) 29-35.
(23) Gu, Z.: Xu, H.; Bin, D.; Yan, B.; Li, S.; Xiong, Z.; Zhang, K.; Du, Y. Preparation of PdNi nanospheres with enhanced catalytic performance for methanol electrooxidation in alkaline medium. *Colloids Surf. A.* 2017, 529, 651-658.
(24) Jiles, D.C. Recent advances and future directions in magnetic materials. *Acta Mater.* 51 (2003) 5907-5939.
(25) Ai, F.; Yao A.; Huang, W.; Wang, D.; Zhang, X.; Synthesis of PVP-protected Pd-Ni nanoalloys by modified polyol process and their magnetic properties. *Physica E* 42 (2010) 1281–1286.
(26) Fujiwara, H.; Tokunaga, T.; Nakajima, A., Magnetocrystalline anisotropy constant K1 of Pd-Ni alloys, *J. Phys. Soc. Japan* 34 (1973) 1104.
(27) Elias, L.; Chitharanjan Hegde, A. Effect of Magnetic Field on HER of Water Electrolysis on Ni–W Alloy. *Electrocatalysis* 8 (2017) 375–382.
(28) Maity, S.; Eswaramoorthy, M. Ni–Pd bimetallic catalysts for the direct synthesis of H2O2 unusual enhancement of Pd activity in the presence of Ni. *J. Mater. Chem. A*, 4 (2016) 3233-3237.
(29) Rai, R. K.; Gupta, K.; Tyagi, D.; Mahata, A.; Behrens, S.; Yang, X.; Xu, Q.; Pathak, B.; Singh, S. K. Access to highly active Ni–Pd bimetallic nanoparticle catalysts for C–C coupling reactions. *Catal. Sci. Technol* 6 (2016) 5567-5579.
(30) Danaee, I.; Shoghi F.; Dehghani Mobarake, M.; Kameli, M., Electrocrystallization of palladium from $Pd(NH_3)_4Cl_2$ bath on stainless steel 316L *J Solid State Electrochem*. 14 (2010) 57-62.
(31) Kumar, K.S.; Haridoss, P.; Seshadri, S.K. Synthesis and characterization of electrodeposited Ni–Pd alloy electrodes for methanol oxidation. *Surf. Coat. Technol*. 202 (2008)1764–1770.
(32) Shao, W.; Zangari, G. Dendritic Growth and Morphology Selection in Copper Electrodeposition from Acidic Sulfate Solutions Containing Chlorides. *J. Phys. Chem. C.* 113 (2009) 10097–10102.
(33) Silva, R.P.; Eugénio, S.; Silva, T.M.; Carmezim, M.J.; Montemor, M.F., Fabrication of three-dimensional dendritic Ni–Co films by electrodeposition on stainless steel substrates. *J. Phys. Chem. C*. 116 (2012) 22425–22431.
(34) Łomot, D.; Karpińsk, Z., Catalytic activity of Pd-Ni in the oxidation of hydrogen for the safety of nuclear power plant. *Pol. J. Chem. Technol.* 18 (2016)15-18.
(35) Cai, W-F.; Pu, K-B.; Ma, Q.; Wang, Y-H., Insight into the fabrication and perspective of dendritic Ag nanostructures. *J. Exp. Nanosci* 12 (2017) 319-337.
(36) Robertson, S.G.; Ritchie, I.M.; Druskovich, D.M., A kinetic and electrochemical study of the zincate immersion process for aluminum. *J. Appl. Electrochem*. 25 (1995) 659–666.
(37) Pearson, T., Pretreatment of aluminum for electrodeposition. *Trans. IMF* 84 (2006) 121-123.
(38) Watanabe, H.; Honma, H., Fabrication of Nickel Microbump on Aluminum using Electroless Nickel Plating. *J. Electrochem. Soc.* 1997, 144, 471-476.
(39) Olson, T.S.; Atanassov, P.; Brevnov, D.A., Electrodeposition of gold particles on aluminum substrates containing copper. *J. Phys. Chem. B*. 2005, 109, 1243-1250.
(40) Usgaocar, A.R.; Groo, C.H., The electrodeposition, magnetic and electrical characterization of Palladium–Nickel alloys. *J. Electroanal. Chem.* 655 (2011) 87-91.
(41) Olvera, S.; Arce Estrada, E.M.; Sanchez-Marcos, J.; Palomares, F.J.; Vázquez, L.; Herrast, P., Effect of the low magnetic field on the electrodeposition of Co_xNi_{100-x} alloys, *Materials Characterization* 105 (2015) 136–143.
(42) Kostevšek, N.; Žužek Rožman, K.; Pečko, D.; Pihlar, B.; Kobe, S., A comparative study of the electrochemical deposition kinetics of iron-palladium alloys on a flat electrode and in a porous alumina template. *Electrochimica Acta* 125 (2014) 320–329.

(43) Mech, K.; Zabinski, P.; Kowalik, R.; Fitzner, K., Voltammetric study of electro-reduction of tetraamminepalladium(II) onto gold electrode, *J. Electroanal .Chem.* 685 (2012) 15–20.
(44) Aguirre, M.C.; Núñez Coavas, H.; Fabietti, L.M.; Urreta, S.E. Nucleation and Growth Mechanisms in Cu−Co Films. *J. Phys. Chem. C.* 120 (2016) 22142-22154.
(45) Romero-Romo, M.; Aldana-González, J.; Botello, L.E.; Montes de Oca, M.G.; Palomar-Pardavé, M., Electrochemical nucleation and growth of Cu onto Au nanopartículas supported on a Si (111) wafer electrode, *J. Electroanal. Chem.* 791 (2017) 1–7.
(46) Sharifker, B.; Hill, G., Theoretical and experimental studies of multiple nucleation. *Electrochim. Acta* 28 (1983) 879−889.
(47) Bewick, A.; Fleischmann, M.; Thirsk, H. R., Kinetics of the electrocrystallization of thin films of calomel. *Trans. Faraday Soc.* 58 (1962) 2200−2216.
(48) Díaz-Morales, O.; Mostany, J.; Borrás, C.; Scharifker, B.R., Current transient study of the kinetics of nucleation and diffusion-controlled growth of bimetallic phases. *Journal Solid State Electrochemistry*, 17 (2013) 345-351.
(49) Aldana-González, J.; Sampayo-Garrido, A.; Oca-Yemha, M.G.M.; Sánchez, W.; Ramirez-Silva, M.T.; Arce-Estrada, E.M.: Romero-Romo, M.; Palomar-Pardave, M., Electrochemical nucleation and growth of Mn and Mn-Zn alloy from leached liquors of spent alkaline batteries Using a deep eutectic solvent. *J. Electrochem. Soc*. 166 (2019) 199-204.
(50) Yang, Y.; Xu, C.; Hua, Y; Wang, M.; Su, Z.; Electrochemical preparation of Ni-La alloys from the EMIC-EG eutectic-based ionic liquid. *Ionics* 2017, 23, 1703–1710.
(51) Rezaei, M.; Tabaian, S.H.; Haghshenas, D.F., Electrochemical nucleation and growth of Pd/PdCo core–shell nanoparticles with enhanced activity and durability as fuel cell catalyst. *J. Mater. Chem. A*, 2 (2014) 4588-4597.
(52) Xu, C.; Zhao, J.; Hua, Y. Electrodeposition of Ni-Mg alloys from 1-butyl-3-methylimidazolium chloride/glycerin eutectic-based ionic liquid. *J. Solid State Electrochem*.2016, 20, 793–800.
(53) Olson, T.S.; Atanassov, P.; Brevnov, D.A., Electrodeposition of Gold particles on Aluminum substrates containing Copper. *J. Phys. Chem. B* 109 (2005) 1243-1250.
(54) Grujicic, D.; Pesic, B., Electrodeposition of copper: the nucleation mechanisms. *Electrochim. Acta* 47 (2002) 2901-2912.
(55) Hultgren, R.; Zapffe, C.A., An X-ray study of the Iron-palladium and Nickel-palladium systems, *Trans. AIME*. 133 (1939) 58-68.
(56) Nagasawa, H., Trace element partition coefficient in ionic crystals. *Science.* 152 (1966) 767-769.
(57) Lin, W.; Spruiell, J. E.; The structure of nickel-palladium solid solutions. *Acta Metall*. 19 (1971) 451–461.
(58) Franke. P.; Neuschütz, D.; Scientific Group Thermodata Europe (SGTE) Pd-Ni. In: Binary Systems. Part 4: Binary Systems from Mn-Mo to Y-Zr. Landolt-Börnstein - Group IV Physical Chemistry (Numerical Data and Functional Relationships in Science and Technology) 19B4. Springer, Berlin, Heidelberg.
(59) Djokić, S.S.; Nikolić, N.D.; Živković, P.M.; Popov, K.I.; Djokić, N.S., Electrodeposition and electroless deposition of metallic powders: a Comparison, *ECS Trans.* 33 (2011) 7-31.
(60) C.S. Barret, T.B. Massalski, Structure of Metals, Pergamon, Oxford, 1980.
(61) Hau, N.Y.; Yang, P.; Liu, C.; Wang, J.; Lee, P.-H.; Feng, S.-P., Aminosilane-assisted electrodeposition of gold nanodendrites and their catalytic properties. *Sci. Rep*. 7 (2017) 39839.

♣♣♣♣

Supplementary Information

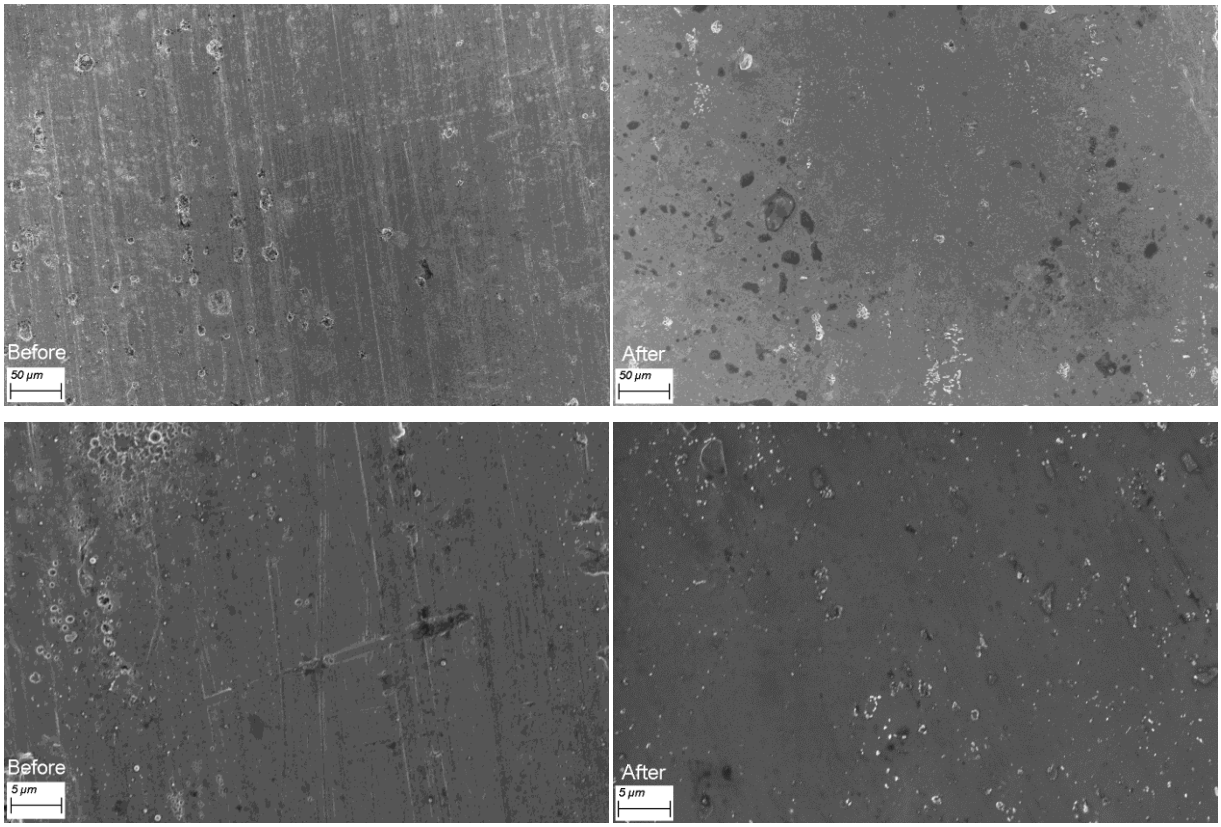

Figure S1: Aluminum substrate surface before (left) and after (right) electro-polishing. The images were taken at similar magnifications than the images shown in Figures 4 – 7 in the main text.

Table S1. Lattice parameter, crystallite size and crystallographic textures T(hkl) calculated for the deposits. A slight (111) preferred orientation is obtained for all the deposits.

Sample	**Lattice parameter a [Å]**	**Scherrer size d_{Sch} [nm]**	**Crystallographic texture T_{hkl}**		
			(111)	**(200)**	**(220)**
Pd70-1.0V	3.81(2)	20(10)	1.27	0.97	0.76
Pd60-1.5V	3.80(2)	30(10)	1.83	0.83	0.84
Pd25-1.0V	3.62(2)	20(10)	1.25	0.99	0.76
Pd15-1.5V	3.60(2)	20(10)	1.30	1.02	0.67

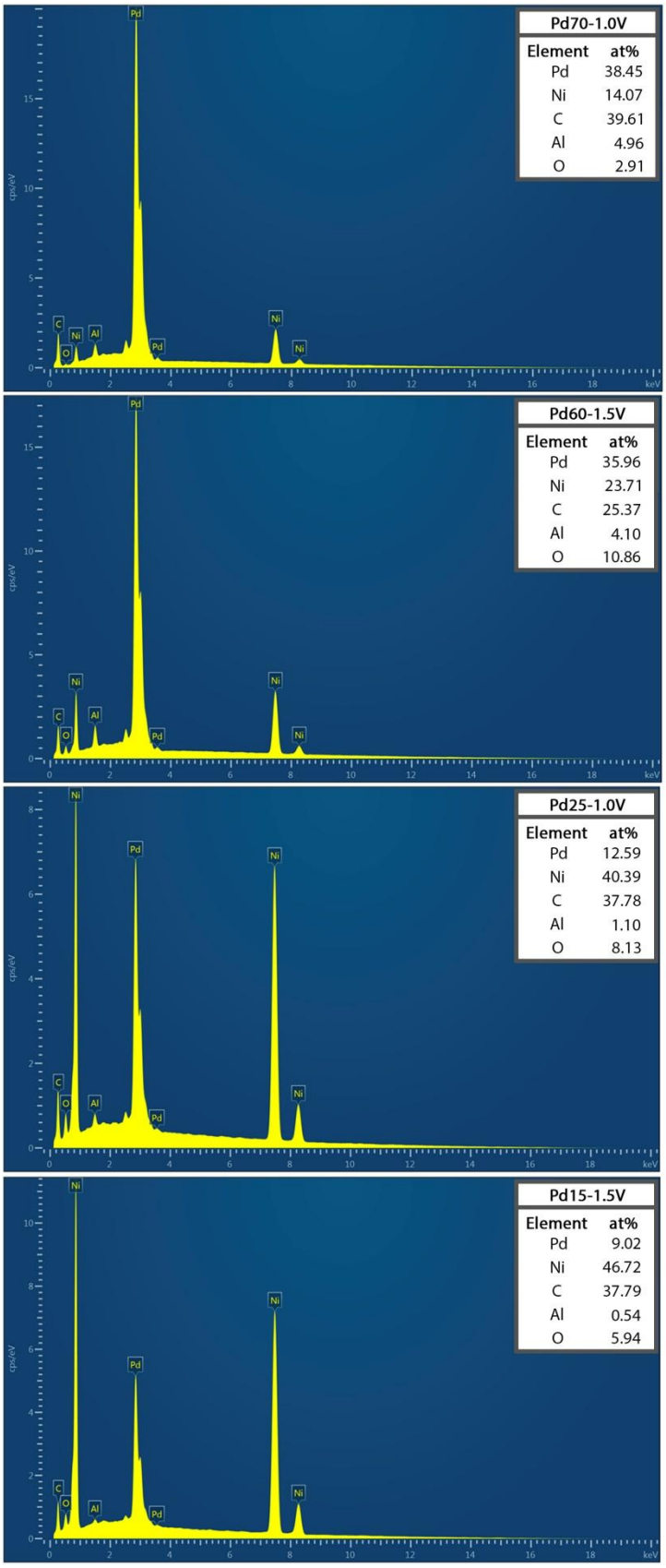

Figure S2: EDS spectra measured with incident beam energy of 20 keV. All elements' contributions are included: Pd and Ni arise from the nanowires; C, Al and O come from the sample holder.

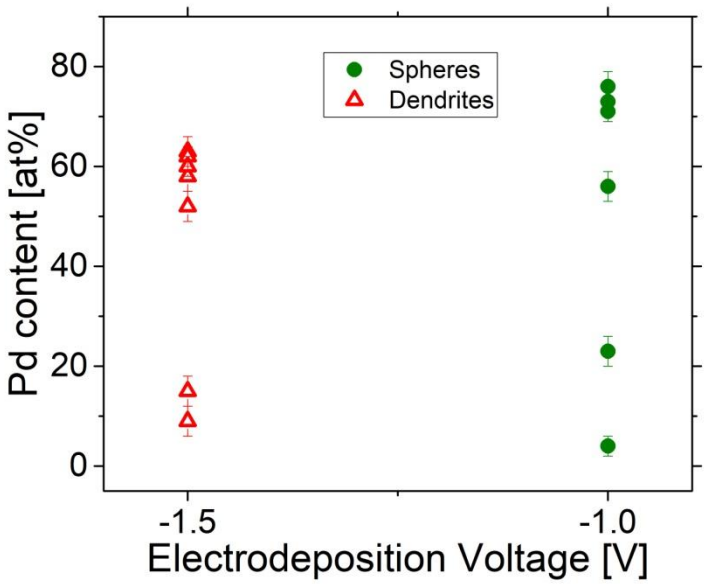

Figure S3: Different samples morphologies according to the electrodeposition voltage and compositions.